OPEN ACCESS

Catalyst Aggregate Size Effect on the Mass Transport Properties of Non-Noble Metal Catalyst Layers for PEMFC Cathodes

To cite this article: Seçil Ünsal *et al* 2023 *J. Electrochem. Soc.* **170** 074502

Journal of The Electrochemical Society, 2023 **170** 074502

Catalyst Aggregate Size Effect on the Mass Transport Properties of Non-Noble Metal Catalyst Layers for PEMFC Cathodes

Seçil Ünsal,[1] Michele Bozzetti,[2] Yen-Chun Chen,[1] Robin Girod,[2] Anne Berger,[3,*] Justus S. Diercks,[1] Sofia Gialamoidou,[1] Jike Lyu,[4] Marisa Medarde,[4] Hubert A. Gasteiger,[3,] Vasiliki Tileli,[2] Thomas J. Schmidt,[1,5,**] and Juan Herranz[1,***,z]**

[1]*Electrochemistry Laboratory, Paul Scherrer Institute, 5232 Villigen-PSI, Switzerland*
[2]*Institute of Materials, Ecole Polytechnique Fédérale de Lausanne, 1015 Lausanne, Switzerland*
[3]*Chair of Technical Electrochemistry, Department of Chemistry and Catalysis Research Center, Technical University of Munich D-85748 Garching, Germany*
[4]*Laboratory for Multiscale Materials Experiments, Paul Scherrer Institute, 5232 Villigen-PSI, Switzerland*
[5]*Laboratory of Physical Chemistry, ETH Zürich, 8093 Zürich, Switzerland*

Non-noble metal catalysts (NNMCs) are regarded as a promising alternative to the costly Pt-based materials required to catalyze the oxygen reduction reaction (ORR) in proton exchange membrane fuel cell (PEMFC) cathodes. However, the large diversity of NNMC synthesis approaches reported in the literature results in materials featuring a wide variety of particle sizes and morphologies, and the effect of these properties on these catalysts' PEMFC performance remains poorly understood. To shed light on this matter, in this work we studied the physical and electrochemical properties of NNMC layers prepared from materials featuring broadly different aggregate sizes, whereby this property was tuned by ball milling the precursors used in the NNMCs' synthesis in the absence vs presence of a solvent. This led to two NNMCs featuring similar Fe-speciations and ORR-activities, but with vastly different aggregate sizes of $>5\ \mu$m vs $\approx$100 nm, respectively. Following the extensive characterization of catalyst layers (CLs) prepared with these materials via electron microscopy and X-ray tomography, PEMFC tests at different loadings unveiled that the smaller aggregate size and $\approx$20% higher porosity of the CL prepared from the wet-milled sample resulted in an improvement of its mass transport properties (as well as a $\approx$2-fold enhancement of its peak power density under H_2/air operation) over the dry-milled material.
 [DOI: 10.1149/1945-7111/ace289]

Manuscript submitted March 15, 2023; revised manuscript received May 16, 2023. Published July 11, 2023.

Supplementary material for this article is available online

The adverse environmental consequences of the extensive use of fossil fuels as a primary energy source can only be reversed through their substitution with renewable energies. Within this prospect, hydrogen is systematically regarded as a key energy carrier excellently suited to store excess renewable electricity,[1] and its re-electrification in fuel cells is also expected to play a crucial role in the transportation sector.[2,3] However, despite significant technological developments over the last decades,[3,4] the cost of the proton exchange membrane fuel cells (PEMFCs) best suited for such transportation applications remains too high for their widespread commercialization. In this regard, significant cost reductions are projected for the majority of the PEMFC-system components thanks to the economy-of-scale (i.e., as the production volume reaches $\geqslant$500,000 automotive PEMFC systems per annum), which on the other hand shall not play a role on the fraction of the costs associated to the expensive Pt-based catalysts implemented in PEMFC electrodes.[5] As a result, such Pt-catalysts are expected to account for $\approx$50% of the PEMFC-stack manufacturing costs, and thus tremendous efforts are being devoted to substitute these costly materials with inexpensive, non-noble metal catalysts (NNMCs), particularly for the more catalytically demanding O_2-reduction reaction (ORR). This body of work has resulted in novel NNMC-synthesis routes that have led to catalysts with initial low current density PEMFC-performances comparable to those of Pt-based catalyst layers (CLs).[6–10] However, NNMCs feature intrinsically lower ORR-activities than Pt, and thus their cathode loadings need to be much higher than those of Pt-based CLs (i.e., $\geqslant$4 $mg_{NNMC}\cdot cm^{-2}$ vs $\leqslant$0.3 $mg_{Pt}\cdot cm^{-2}$, respectively). This in turn results in thick NNMC layers (often $\geqslant 100\ \mu$m vs $\leqslant 10\ \mu$m for Pt-based CLs) that can suffer from mass transport issues[11] that prevent them from reaching the high current densities at as-high-as-possible-potentials that are required for high power (e.g., automotive) applications.

In order to enhance mass transport and facilitate water removal along such thick CLs, it is crucial to increase their porosity (in turn decreasing the tortuosity in the pore phase) while keeping in mind that this can cause an increase of the tortuosity of the proton-conductive ionomer phase that would consequently hinder proton (H^+)-conduction within the CL.[12] Therefore, the optimization of the CL morphology is important to achieve enhanced mass transport properties while retaining sufficient H^+-conductivity.[13] With this motivation, a number of recent studies have focused on improving the high current density performance through a control of the NNMC morphology that can be achieved by tuning the catalyst's aggregate size.[14–17] As an example of this, Ratso et al.[16] achieved a >4–fold improvement in fuel cell performance by tuning the aggregate size and morphology of their NNMCs through adjustments in the ball milling conditions used in their synthesis. Similarly, Uddin et al.[17] also attained a precise control of their metal−organic-framework (MOF-) derived NNMC aggregate size by adjusting the solvent-to-precursor ratio in their synthesis, ultimately achieving a maximum power density of $\approx$600 $mW\cdot cm^{-2}$ using H_2 and air as the cell reactants. Interestingly, many researchers in the field have attempted to improve the PEMFC-performance at high current densities by increasing the NNMCs' meso-porosity,[11,18] but a very high performance (i.e., current densities of $>1.5\ A\ cm^{-2}$ with a peak power of $570\ mW\ cm^{-2}$ using air as the cathode reactant) was recently reported for a highly microporous NNMC with >90% of its pores within the <2 nm range.[7] This result highlights the importance of tailoring the design of each NNMC layer as to improve its transport characteristics and maximize its fuel cell power output.

Among NNMCs, those of the iron−nitrogen−carbon (Fe−N−C) kind commonly feature the best initial PEMFC-performance, and (as already hinted above) are often prepared using MOFs as porosity

*Electrochemical Society Student Member.
**Electrochemical Society Fellow
***Electrochemical Society Member.
[z]E-mail: juan.herranz@psi.ch

precursors.[7–9] However, the use of such costly MOFs is likely to jeopardize the presumed cost advantages of NNMCs over Pt-based materials. With this motivation, our group recently presented a novel NNMC synthesis approach that relies on the use of inexpensive precursors (i.e., polyacrylonitrile and Na_2CO_3)[19] and yielded NNMCs with a relatively high initial ORR-activity in PEMFC tests ($\approx$14 A·g_{NNMC}^{-1} at 0.8 V in H_2/O_2 at 80 °C, 1.5 bar_{abs}, and 100% relative humidity) but a poor high current density performance. In the same study,[19] those poor mass transport properties were hypothesized to stem from the catalyst's large aggregate size ($\geqslant$2 μm). Specifically, for those highly microporous NNMCs (with $\approx$ 1000 $m^2\,g^{-1}$ of microporosity), such large aggregates would translate in an abundancy of deep micropores and correspondingly long diffusion paths for the O_2 and H_2O consumed and produce at the catalyst's ORR-active sites, which are generally believe to be hosted inside its micropores.[20–23]

Thus, in this study we aimed to decrease the large size of these aggregates by modifying the ball milling (BM) conditions through the inclusion of a solvent in the BM-step of the NNMCs' synthesis (i.e., using wet BM).[24] Our electrochemical characterization of the resulting materials with different aggregate sizes showed that they possess similar mass-specific ORR-activities. The porosity and uniformity of their CLs were assessed using focused ion beam scanning microscopy (FIB-SEM) tomography and X-ray tomographic microscopy (XTM), and the distribution of ionomer across the CLs was evaluated by transmission electron microscopy (TEM). We then conducted PEMFC measurements using O_2 or air as the cathode feed for different catalyst loadings (from 1 to 6 $mg_{NNMC}\,cm^{-2}$), and performed a careful overpotential deconvolution of the acquired polarization curves from which we quantified the effect of aggregate size and catalyst loading on the CLs' mass transport properties. While increasing the loading of wet-milled CLs from 1 to 4 $mg_{NNMC}\,cm^{-2}$ significantly decreased the mass transport overpotential, higher loadings led to additional mass transport losses in the case of the dry-milled catalyst with a larger aggregate size. These differences are hypothesized to be caused by the corresponding disparities in the spatial locations of the ORR-actives sites in these catalysts along their largely differing aggregates (and the pores within them).

Experimental

Catalyst synthesis.—The NNMCs were prepared using a synthesis approach discussed in detail in the supplementary information and based on the one presented in our previous publication.[19] In brief, it consists of five main steps: (i) mixing of polyacrylonitrile, Na_2CO_3 and Fe-phenanthroline precursors in DMF, followed by their subsequent drying overnight; (ii) ball milling (BM) of the resulting powder to decrease its particle size; (iii) a first heat treatment (HT) at 700 °C; (iv) an acid washing step in 1 M H_2SO_4 at 80 °C; and (v) a second HT at 950 °C, Notably, the three NNMCs featured in this work prepared by changing the BM condition in the second steo of the synthesis, while the remaining steps were similar for all samples. For the "dry BM-5 mm" sample, BM was performed with 5 mm diameter ZrO_2 balls, with 8 cycles (each lasting 10 min and with a 5 min break in-between cycles) at 300 rpm and with a balls/powder mass ratio of 4.45, while for the "dry BM-3 mm" sample, 3 mm diameter balls and a balls/powder mass ratio of 27 were used for 16 h of non-stop milling at 150 rpm. For the "wet BM-x" samples (where x represents the ball size of 1, 2, 3, or 5 mm), the same milling conditions as with the "dry BM-3 mm" sample were used, but with the addition of 10 ml of ethanol in the BM jar.

Physical characterization of the NNMCs and electrochemical RDE-testing.—A detailed description of the procedures used for the physicochemical characterization and electrochemical testing of the catalyst in rotating disk electrode (RDE) configuration can be found in the supplementary information. In brief, the Fe-content in the final samples was obtained by inductively coupled plasma optical emission spectrometry (ICP-OES). The surface areas of all catalysts were determined by N_2-physisorption measurements. Scanning electron microscopy (SEM) images were acquired in a Carl Zeiss Ultra 55 SEM, using the in-lens detector. Ex situ X-ray absorption spectroscopy (XAS) measurements were carried out at the SuperXAS (X10DA) beamline of the Swiss Light Source (SLS). The electrochemical RDE measurements were performed in 0.1 M $HClO_4$ electrolyte saturated with N_2 or O_2 using catalyst loading of $\approx$500 $\mu g_{NNMC}\,cm^{-2}$.

MEA fabrication.—The membrane electrode assemblies (MEAs) were prepared using a commercial gas diffusion electrode (GDE − Johnson Matthey, 0.4 $mg_{Pt}\,cm^{-2}$ HISPEC 9100 Pt/HAS on a 1 × 1 cm^2 piece of Sigracet 25 BC gas diffusion layer) as the anode and hot pressing this GDE at 140 °C for 2 min at 10 bar on a piece of Nafion® HP membrane (Ion Power) as to obtain a half-MEA, as previously described by Yin et al.[25] This half-MEA was then placed on a plate heated at 60 °C with the anode GDE in contact with the plate and the opposite part of the membrane facing upwards. The cathode catalyst ink was prepared by mixing the NNMC of choice with a solution of isopropanol and ultrapure water (in a 3:7 volume ratio) in the proportions needed to yield an NNMC/solvents ratio of 9 $mg_{NNMC}\,mgml_{H2O+IPA}^{-1}$, as well as the volume of Nafion® ionomer solution required for reaching an ICR of 0.6. After the ink was sonicated for 30 min, it was sprayed onto the upper side of the half-MEA using an automated ultrasonic spray coating system (Sono-Tek) at a flow rate of 0.05 ml mgs^{-1} and with a sonicator-tip-to-sample distance of 2.5 cm until the targeted cathode catalyst loading (ranging from 1 to 6 $mgmg_{NNMC}\ cm^{-2}$) was achieved. For each fuel cell tests, at least 2 electrodes were prepared, and the loadings were determined by weighing the sample with a microbalance before and after spraying (in the latter case, following the complete drying of the corresponding electrode). We have to note that the mass of the Nafion membranes can significantly change between the first and second weighing due to variations in the relative humidity of the environment, an thus the obtained mass difference can result in an inaccurate catalyst loading. To overcome this issue, the mass of the sprayed and dry membrane was corrected with the relative weight change of a reference, half MEA whose mass was recorded at the same times as that of the original membrane used for the preparation of the electrode and the corresponding electrode (i.e., before and after spraying).[26] The thickness of the resulting cathode catalyst layers was measured at five different points for each MEA using a Mitutoyo MCD-25PX dial gauge with a nominal accuracy of ±1 μm. Lastly, a gas diffusion layer (GDL, Sigracet SG29BC) was placed onto the NNMC layer prior to the cell assembly.

Characterization of the catalyst layers.—The NNMC-layers were characterized by focus ion beam scanning electron microscopy (FIB-SEM) tomography, X-ray tomographic microscopy (XTM) based on a laboratory-computed tomography (CT) scanner, phoenix nanotom (General Electric, Germany), and transmission electron microscopy (TEM). The detailed experimental procedures related to each of these methods are given in the supplementary information. Briefly, structural details (e.g., porosity, tortuosity) of the NNMC layers were obtained by 3D FIB-SEM nanotomography while XTM-CT was used to determine the thickness as well as the porosity of NNMC layers. The distribution of the ionomer across selected NNMC layers was determined by TEM imaging and elemental analysis of microtomed cross-sections of the MEAs. In addition, the electrical resistance of the NNMC layers was obtained through a 4-point-probe measurement,[27] for which the experimental details can again be found in the supplementary information.

PEMFC tests.—The PEMFC tests were performed in a differential fuel cell[28] with an active area of 1 cm^2. After completing the assembly by placing the GDL onto the NNMC layer, the resulting MEA was placed inside the cell and compressed by selecting the

total thickness of the gaskets that would result in a ≈25% compression of the diffusion media (i.e., cathode GDL and anode GDE, under the assumption that catalyst- and microporous-layers are uncompressible). The polarization curves were recorded galvanostatically, holding the current at selected values over 90 s, starting from the open circuit voltage (OCV) and progressing to higher current densities, so that reported potentials correspond to the average values during the last 30 s of each current hold. All polarization curves were obtained at 80 °C, 1.5 bar_{abs} and 100% relative humidity (RH), with anode H_2 (Pangas 5.0) and cathode O_2/Air (Messer AG, 5.5) using flow rates of 600 and 1000 ml mg min^{-1}, respectively. After each measurement at a given current, the corresponding high frequency resistance (HFR) was determined by galvanostatic electrochemical impedance spectroscopy (GEIS) with a 10% current perturbation in a frequency range of 1 MHz to 500 mHz and with 6 points per decade.

Mass-normalized ORR-activities (MAs) were interpolated within the linear regime of the corresponding Tafel plots. For the H_2/Air measurements, the directly interpolated MAs at 0.8 V ($i_{kin,air}$) were corrected for the concomitant deviation from an O_2 partial pressure (p_{O2}) of 1 bar using the following equation:

$$i_{kin,o2} = i_{kin,air} \cdot \left(\frac{p_{o2}}{p_{air}}\right)^m \quad [1]$$

where p_{O2} and p_{air} correspond to 0.21 and 1 bar, respectively, and m is the reaction order of the ORR with regard to the oxygen partial pressure at constant electrode potential (i.e., including both thermodynamic and kinetic contributions), for which we assumed a value of 0.79 based on what was reported by Neyerlin et al.[29] for Pt-based catalysts.

In order to determine the H^+-conduction resistance in the CLs, potentiometric electrochemical impedance spectroscopy (PEIS) tests at 0.2 V (with a 5 mV perturbation) between 500 mHz to 1 MHz were performed while operating the PEMFC at 80 °C with fully humidified H_2 and N_2 feeds at the anode and cathode, respectively.[30] The spectra were fitted to the transmission line model (TLM) (with $X^2 < 0.005$) by using Z-fit provided in the EC-Lab® V11.36 software package. All tests were performed with a Bio-Logic VSP-300 potentiostat equipped with a 10 A/5 V current booster.

Results and Discussion

NNMCs' physical characterization.—In order to decrease the large aggregate size of the NNMC obtained in our previous work[19] (corresponding to the "dry BM-5 mm" sample in Fig. 1a, and featuring >2 μm large aggregates), we modified the BM conditions of the precursors' BM in the second step of the synthesis of these catalysts (see the Experimental section for details). Since small ball sizes and high ball/powder mass ratios combined with a sufficient milling duration are known to improve milling efficiency,[24,31–33] we first decreased the ball size from 5 to 3 mm while increasing the balls/precursor mass ratio from 4.45 to 27 and performing 16 h of milling. Although this change in the BM procedure resulted in a partial reduction of the final catalyst's average aggregate size (see the SEM image of the "dry BM-3 mm" sample in Fig. 1b), some large aggregates up to 5 μm in diameter were still visible in this material. Therefore, we proceeded to substitute the dry BM originally used to mix the precursors with wet BM, whereby the addition of a solvent reportedly improves the milling efficiency by reducing the surface energy of the particles.[24,34] As shown in Fig. 1c (see "wet BM-3 mm" sample), this wet BM resulted in an NNMC with an aggregate size within the ≈100 s of nm range and completely devoid of the larger aggregates featured by its dry BM analogues. Notably, varying the size of the balls used for wet BM from 1 to 5 mm did not result in significant changes in the size or morphology of the resulting catalysts, as shown in Fig. S1. Moreover, images with a larger magnification (see the inset in Fig. 1c and Figs. 1Se–1h) unveil the presence of nano-tubes in all wet-milled samples, likely due to the existence in these NNMCs of carbon-encapsulated Fe-based particles that are known to act as seeds for the growth of such nano-tubes at the high temperatures[35] required for these materials' synthesis.

Following this assessment of the NNMCs' morphology, we proceeded to determine their specific surface area by N_2-sorption measurements, and thus their corresponding total and microporous surface areas are listed in Table I. In agreement with our previous work,[19] the "dry BM-5 mm" sample with larger aggregates possesses a very high surface area of ≈900 $m^2\ g^{-1}$, of which ≈90% corresponds to micropores with < 2 nm in width. Complementarily, decreasing the ball size to 3 mm while keeping dry milling did not affect significantly the total N_2-sorption area, but the fraction of it corresponding to micropores decreased to ≈50%, probably because the enhanced milling efficiency led to the appearance of additional mesopores in this "dry BM-3 mm" sample. By comparison, the "wet BM-3 mm" sam(≈1100 $m^2\ g^{-1}$) of which ≈70% corresponds to micropores. On top of this, Table I also includes all three NNMCs' Fe-contents. In this regards, it is worth noting that the "dry BM-5 mm" sample possesses a significantly smaller amount of Fe than the analogous material featured in Ref. 36 (≈1 wt% Fe here vs ≈3 wt% Fe in Ref. 36) due to the harsher acid washing conditions used in this work as compared to Ref. 36 (4 h in 1 M H_2SO_4 at 80 °C here vs overnight in 0.1 M $HClO_4$ at room temperature). On the other hand, the two NNMCs prepared with 3 mm balls under dry or wet conditions feature higher and resembling Fe-contents of ≈2 wt %. We hypothesize that this difference in Fe-contents may stem from an effect of the aggregate size on the distribution and/or nature of the catalysts' Fe-species prior to their syntheses' acid-washing step, whereby the iron in the larger particles of the "dry BM-5 mm" sample would be more prone to dissolution (e.g., due to an incomplete encapsulation with a protective C-shell).

In order to investigate whether the Fe-speciation of these NNMCs is affected by the changes in the BM-conditions, we further characterized the three catalysts by performing XAS-measurements at the Fe K-edge. Their Fourier transformed (FT-) extended X-ray absorption fine structure (EXAFS) spectra (within the range 3 ⩽ k ⩽

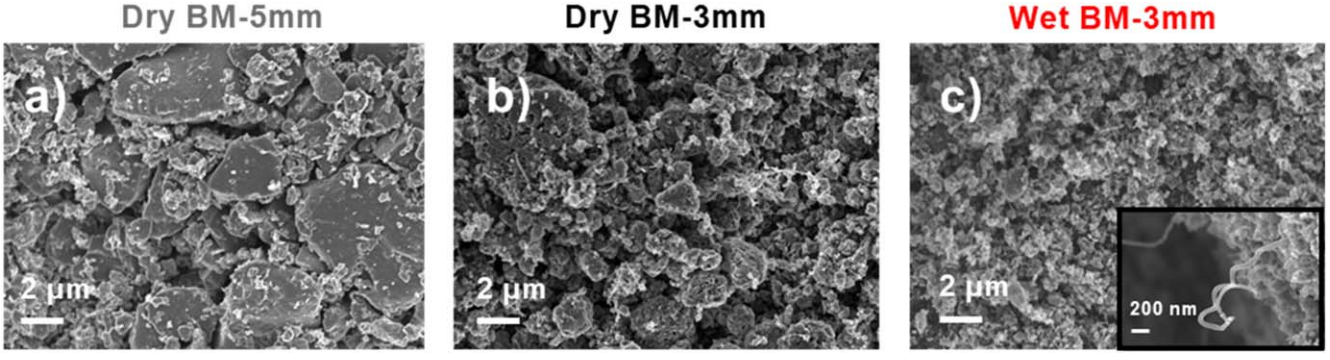

Figure 1. Scanning electron microscopy images of the dry- and wet-milled NNMCs prepared with different ball sizes.

Table I. Summary of the Fe-contents (inferred from ICP measurements of aliquots of the solutions used to acid-digest each catalyst) and total vs microporous surface areas of the different NNMCs included in this study.

	Fe content (wt%)	Total surface area ($m^2 \cdot g^{-1}$)	Microporous surface area ($m^2 \cdot g^{-1}$)
Dry BM-5mm	1.1 ± 0.2	888	716
Dry BM-3mm	2.0 ± 0.1	860	458
Wet BM-3mm	1.8 ± 0.2	1072	766

10 $Å^{-1}$) displayed in Fig. 2a closely resemble each other over the complete k-range, indicating a similar Fe-coordination environment for the three NNMCs. Specifically, all NNMCs' FT-EXAFS spectra display a major scattering component at an uncorrected radial distance of ≈2 Å, that can be assigned to Fe−Fe scattering based on the comparison with the FT-EXAFS spectrum of Fe-foil (Fig. 2b). This can in turn be ascribed to an Fe-speciation preponderantly dominated by Fe-based (nano)particles, in good agreement with our previous observations for NNMCs prepared in a similar way as the "dry BM-5 mm" sample,[36] and also consistent with the enhancing role of such species in the formation of the carbon nanotubes spotted in the catalysts' SEM images discussed above (cf Fig. 1c). Nevertheless, the FT-EXAFS spectra also feature a non-negligible scattering contribution at a non-corrected radial distance of ≈1.5 Å, assignable to the coordination of Fe by light scatterers like O, C and/or N, and can therefore be attributed to the heme-like, N-coordinated Fe-sites that are generally regarded as the ORR-active centers in these materials.[37–39] In order to better assess this important aspect, Fig. 2c displays the NNMCs' normalized XANES spectra along with those of FeN_x-sites and Fe_3C-like species, in turn derived from a multivariate curve resolution (MCR) analysis of a series of catalysts similar to the "dry BM-5 mm" sample featured in Ref. 40. We then used these base-components' spectra to linearly fit the NNMCs' XANES (see Fig. S2), as to obtain the fraction of Fe featured in the form of FeN_x-sites summarized in Fig. 2d. Notably, decreasing the ball size from 5 to 3 mm in the dry milling syntheses led to a ≈50% increase in the Fe–N_x content of the corresponding NNMCs, whereas the fraction of such Fe–N_x sites remained similar (at ≈25% of the total atomic Fe-inventory) for the dry- and wet-BM catalysts prepared with 3 mm balls, thus indicating that the wet-milling decreased the particle size without effecting the net Fe-speciation.

NNMCs' electrochemical characterization.—The electrochemical performance of the different NNMCs was first studied with RDE voltammetry measurements (see the Supplementary Information for experimental details, and Fig. S3 for an example of the procedures of capacitive- and ohmic-compensation[41]), whereby the polarization curves and corresponding Tafel plots obtained with this technique are displayed in Figs. 3a and 3b, respectively. Interestingly, the dry-milled samples (i.e., "Dry BM-5 mm" (gray) and "Dry BM-3 mm"(black)) display poorly defined current plateaus at potentials < 0.6 V vs RHE, while the wet-milled catalyst ("wet BM-3 mm" (red)) features a true limiting current with a value that is in line with what is experimentally observed for the 4-electron reduction of O_2 to H_2O on Pt-based electrodes (i.e., in 0.1 M $HClO_4$ at 23 °C and 1600 rpm, $i_{lim} \approx -$ 6 mA cm^{-2}).[42,43,44] Notably, the fact that the wet-milled catalyst reaches such a high limiting current may appear surprising, since the catalyst loadings used in these RDE-measurements entail » 1 μm thick CLs that are expected to suffer from O_2-concentartion gradients along their thickness, and that would therefore lead to limiting current values below those attained on flat or thin film RDEs.[45,46] However, as discussed in a recent study featuring these three NNMCs,[41] this high limiting current of the wet-milled CL can result from a regeneration of O_2 along its thickness, in turn caused by the disproportionation of H_2O_2 arising from the ORR into H_2O and O_2.[47] Correspondingly, the lower limiting currents featured by the two dry-milled samples would be the result of a lower extent of H_2O_2-disproportionation

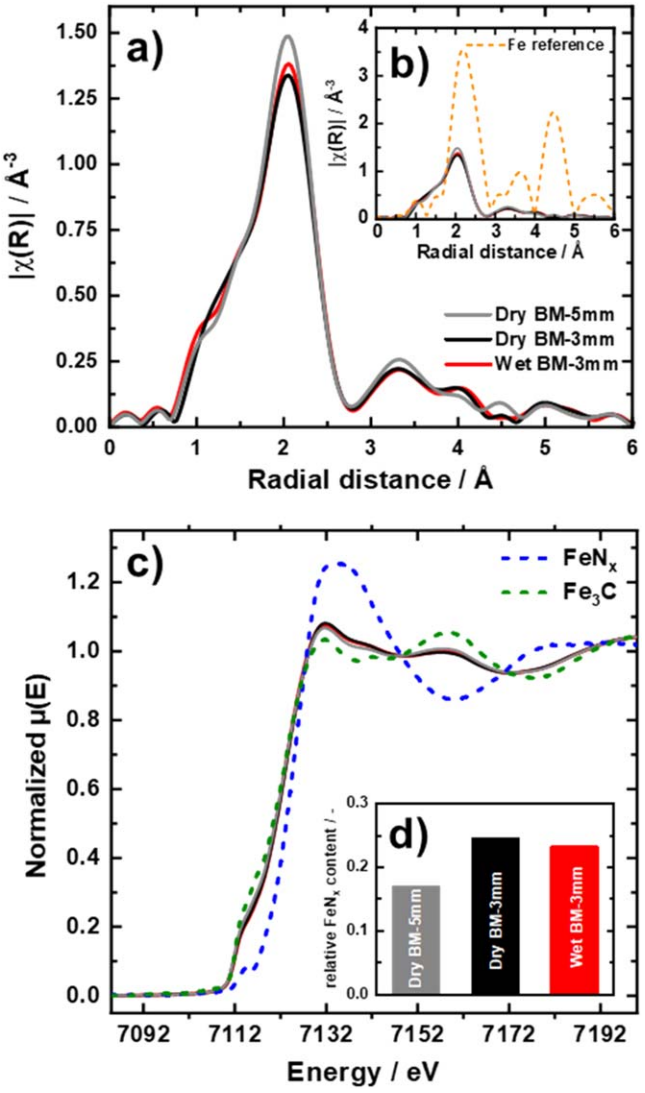

Figure 2. Fourier-transformed (FT-) EXAFS spectra of the NNMCs (a) and their comparison with the spectrum of Fe-foil (b). Normalized Fe K-edge XANES spectra of the different NNMCs, along with two spectral components representing FeN_x-sites and Fe_3C, derived from the multivariate curve resolution analysis in Ref. 40 (c). Relative contents of FeN_x-sites (with regards to the total number of Fe-atoms in the sample) in the three NNMCs derived from linear combination fits of their XANES spectra based on the spectral components of FeN_x-sites and Fe_3C in Fig. 2c (d).

along their CL-thicknesses stemming from catalyst-specific differences in the residence time of this H_2O_2 within the CLs (tied to their porosity and tortuosity), and/or from the amount and distribution of Fe-species that possibly catalyze H_2O_2-dispoportionation.[48]

Beyond these discrepancies, when Eq. S1 is used to transform the measured currents into kinetically-controlled ones, similar mass activities of ≈1.0–1.5 A g_{NNMC}^{-1} at 0.8 V vs RHE are derived for all three catalysts based on their Tafel plots in Fig. 3b. In the case of

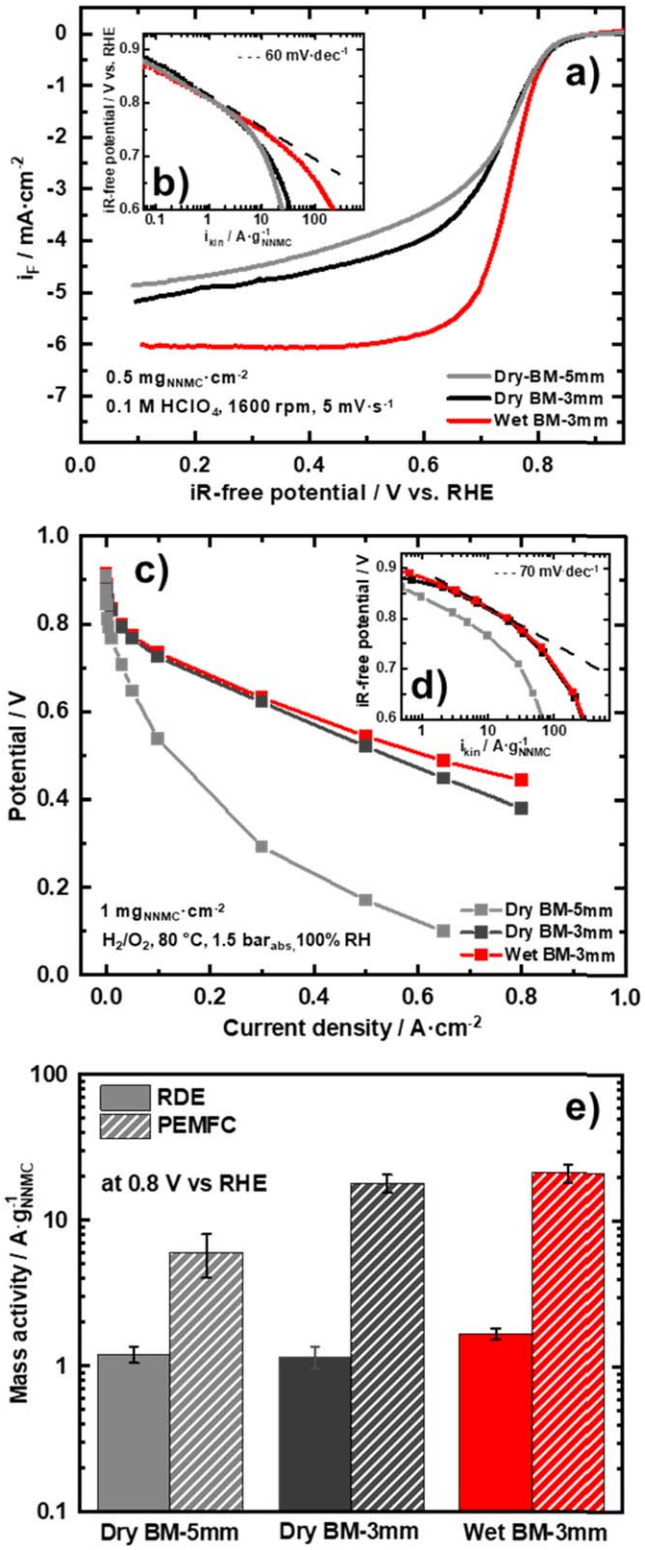

Figure 3. Ohmically- and capacitively-corrected polarization curves obtained through RDE- voltammetry positive-going scans) in O_2-saturated 0.1 M $HClO_4$ at 1600 rpm, 25 °C and 5 mV s^{-1} for the different NNMCs at a loading of 0.5 mg_{NNMC} cm^{-2} (a) and corresponding Tafel plots (b). H_2/O_2 polarization curves measured in a PEMFC at 1.5 bar_{abs}, 80 °C and 100% relative humidity (RH) for the MEAs fabricated with the different NNMCs at a loading of 1 mg_{NNMC} cm^{-2} (c) and corresponding Tafel plots (d). Summary of the mass-specific ORR-activities at an iR-corrected potential of 0.8 V in RDE vs PEMFC tests (obtained from panels b vs d, respectively) (e).

the "dry BM-5 mm" sample, this mass activity agrees well with what was reported[40] for a similarly prepared NNMC with resembling FeN_x- and final Fe-contents (≈20% and 1.1 wt% Fe herein, vs ≈40% and 1.3 wt% Fe for the fully[57]Fe-enriched NNMC in Ref. 40). Moreover, the wet-milled samples prepared with different ball sizes also displayed enhanced limiting currents but similar mass activities in RDE measurements (≈1.5 $A.g_{NNMC}^{-1}$ − see Figs. S4a and S4b), which are additionally comparable to the mass activities of various NNMCs synthesized by different groups and reportedly within the range of 0.6 to 3.3 $A.g_{NNMC}^{-1}$ at 0.8 V vs RHE.[49]

Although RDE is very well suited for a quick screening of the ORR-activity of NNMCs, the values derived from this technique are commonly well below those measured in the actual PEMFC environment.[20] Therefore, we also evaluated the fuel cell performance of the different NNMCs with H_2 and O_2 as the reactants and with a catalyst loading of 1 mg_{NNMC} cm^{-2}. As shown in Fig. 3c, the decrease of the NNMCs' aggregate size brought along by the change of the BM conditions resulted in a profound improvement of the PEMFC performance. Specifically, compared to the "dry BM-5 mm" sample, the "wet BM-3 mm" and "dry BM-3 mm" catalysts feature a ≈4-fold enhancement in current density at potentials ⩽0.6 V, while no significant differences are observed between the polarization curves of these two catalysts recorded under H_2/O_2 and at the low loading of 1 mg_{NNMC} cm^{-2} used in these tests. Moreover, the wet-milled samples prepared with different ball sizes also displayed a similar PEMFC performance as the "wet BM-3 mm" catalyst (Fig. S5). Notably, the ordering among the samples' high current density performance in these H_2/O_2 PEMFC tests (whereby "wet BM-3 mm" ≈ "dry BM-3 mm" > "dry BM-5 mm") somehow contradicts what was observed in the RDE measurements (where "wet BM-3 mm" > "dry BM-3 mm" ≈ "dry BM-5 mm"—cf Fig. 3a and the discussion above). This inconsistency may stem from a differing sensitivity of these aggregate size and mass transport effects to the reaction environments encountered in RDE and PEMFC tests. More precisely, RDE vs- PEMFC-measurements imply O_2-diffusion within liquid vs gaseous phases (whereby the latter entails a ≈5 orders of magnitude larger diffusion coefficient), and thus our results suggest that gaseous O_2-diffusion mostly improves upon transitioning from the large aggregates in "dry BM-5 mm" (possessing longer diffusion paths) to the mid- and small-sized ones in "dry BM-3 mm" and "wet BM-3 mm" (implying diffusion over shorter distances). On the other hand, in the liquid media of RDE tests, the main improvement is observed for the smaller aggregates in the "wet BM-3 mm" catalyst (possessing smaller diffusion path). However, as discussed above, the diffusion limited currents observed in these RDE measurements are likely also affected by material- and/or CL-specific differences in the extents of H_2O_2-dispropotionation that are hardly amenable to the PEMFC environment and further complicate the comparison between the results in these different media.

Leaving these differences aside, the mass-normalized ORR-activities at 0.8 V inferred from the Tafel plots in Fig. 3d are similar for the "dry BM-3 mm" and "wet BM-3 mm" NNMCs (≈20 A g_{NNMC}^{-1}), and ≈4-fold larger than the value of ≈5 A g_{NNMC}^{-1} displayed by the dry BM-5 mm sample. The latter is in turn ≈3-fold lower than what was reported for a similarly prepared sample in our previous work[19] (≈14 A g_{NNMC}^{-1}); as discussed above, though, this difference is possibly caused by a lower number of ORR-actives sites in the "dry BM-5 mm" sample, in terms due to the harsher acid washing conditions involved in the preparation of the catalysts in the present study as compared to the one in Ref. 19 (i.e., 1 M H_2SO_4 at 80 °C in this work vs 0.1 M $HClO_4$ at room temperature in Ref. 19).

A complete comparison among mass normalized ORR-activities derived from RDE vs PEMFC measurements (extracted from Figs. 3b and 3d, respectively) is given in Fig. 3e. As briefly discussed above, the ≈5 to ≈20-fold difference between the ORR mass activities at 0.8 V obtained in the PEMFC measurements as

compared to the RDE tests for all samples are a common feature in the literature,[50,51] and could (partially) be related to the differences in the temperatures at which the two types of measurement are performed (≈25 vs 80 °C for RDE vs PEMFC, respectively) and/or to the differences in catalyst ink compositions (i.e., an ICR of 0.3 in RDE but of 0.6 in the PEMFC). Since optimum PEMFC-performances are commonly obtained with an ICR of ≈0.6,[7,52] we used this value for all the PEMFC tests reported in this study, and instead verified the effect of the ionomer content on the activity derived from RDE tests by varying the ICR in those measurements between 0.3 and 1 for the "wet BM-3 mm" sample. While we did not observe any improvement in the mass activity upon increasing the ICR from 0.3 to 0.6 (with both values leading to $\approx 1\ A\ g_{NNMC}^{-1}$—see Fig. S6a), a further increase to an ICR of 1.0 significantly deteriorated the mass activity (Figs. S6b and S6c), even if this did not lead to any significant changes in the capacitive currents (Fig. S6d). Notably, this lower ORR-activity at a high ICR can be expected, as it can lead to an additional ionomer film resistance[45,46] caused by the presence of excess ionomer. Alternatively, Jaouen et al. also observed a similar decay of the RDE mass activity at ICR-values ⩾1.0 for an NNMC, and hypothesized that the resembling lack of changes in the capacitive currents at all ICRs may result from a balancing between increased currents for some particles and a loss of electrical contact for others due to their complete encapsulation with ionomer.[50]

Beyond this possibility, and since we could not explain the activity difference between RDE and PEMFC tests based on their difference in ionomer content, we then verified the performance of the "wet BM-3 mm" sample in an RDE test at 50 °C (Fig. S7). This higher temperature led to a ≈80% increase of the mass activity with regards to the room temperature value (see Fig. S7c) from which we calculated an apparent activation energy at a constant iR-free voltage of 0.8 V vs RE and a fixed O_2-concentration of 1 mm of $\approx 30\ kJ\ mol^{-1}$ using the Arrhenius relation.[50] This value is comparable to the activation energies reported in the literature for different Fe-based NNMCs, varying between $9 - 50\ kJ\ mol^{-1}$ at potentials varying between 0.6 V vs RHE and E_{rev}.[50,53,54] However, if the ≈20-fold difference in ORR-activities at 0.8 V measured in PEMFC vs RDE (at 80 vs 25 °C, respectively) were to only stem from a temperature difference, a significantly larger activation of $\approx 47\ kJ\ mol^{-1}$ would be expected. Since the latter value is much higher than the $\approx 30\ kJ{\cdot}mol^{-1}$ derived from the RRDE tests at 50 and 25 °C, a mere temperature difference cannot completely explain the ≈20-fold larger ORR-activity observed in RDE vs PEMFC measurements. While fully understanding the origin of this difference remains beyond the scope of this manuscript, several reasons for this large gap between RDE- and PEMFC-derived ORR-activities have been discussed in the literature[20,50,51] (e.g., the use of liquid vs solid electrolytes and/or the factors that govern mass transport limitations in either media).

Properties of the NNMC layers.—Due to the poor PEMFC performance of the "dry-BM-5 mm" sample in the H_2/O_2 measurements displayed above (cf Fig. 3c), we now focus our attention on the CLs prepared with the "dry BM-3 mm" and "wet BM-3 mm" samples, featuring similar ORR-activities and overall performances in the H_2/O_2 fuel cell tests (*vide supra*). It has to be noted that besides the morphology of the catalyst powder, the uniformity of the corresponding CLs can also have a significant impact on the PEMFC performance, even if most works in the NNMC field do not consider this aspect. In this regard, a recent cross-sectional tomography study revealed a significant variation (i.e., a standard deviation >30 μm) in the thickness of a highly loaded ($4\ mg_{NNMC}\ cm^{-2}$) NNMC layer with high tortuosity.[55] Therefore, we first aimed to confirm the uniform thickness of the CLs with various NNMC-loadings and fabricated with the "dry BM-3 mm" and "wet BM-3 mm" samples. These averaged thicknesses are based on measurements in at least five different locations and with a high-precision dial gauge and (for selected samples) by SEM of freeze-cracked CCMs or direct XTM of the corresponding MEAs, and are listed in Table SI. Notably, the thicknesses obtained with the high-precision dial gauge are in line with the values obtained by cross-section SEM (Fig. S8) and XTM (Fig. S9), which additionally proves that the automated spraying resulted in CLs with a uniform thickness (i.e., with standard deviations <10 μm). Moreover, based on the loading and thicknesses of the "wet BM-3 mm" CLs in Table SI, this sample features a loading-normalized thickness of $\approx 25\ \mu m/(mg_{NNMC}\ cm^{-2})$ that is in very good agreement with the value calculated for another NNMC layer with a similar ICR[51] (i.e., $\approx 32\ \mu m/(mg_{carbon}\ cm^{-2})$, based on the values reported in Table II of Ref. 51).

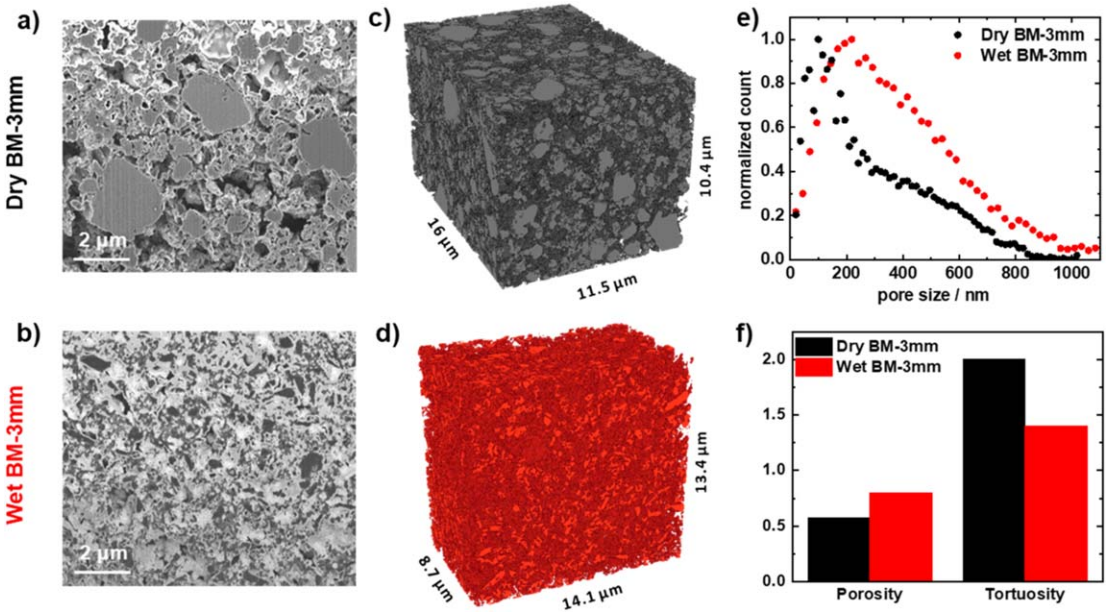

Figure 4. FIB-SEM cross-sectional images of ZnO-filled catalyst layers prepared with the dry BM-3 mm (a) and wet BM-3 mm (b) samples. 3D reconstructions of the CLs prepared with the dry BM-3 mm (c) vs wet BM-3 mm (d) NNMCs, whereby the brighter regions in the volumes correspond to the external surfaces and the darker regions represent the inner surface of the pore network. Corresponding pore size distributions (e), porosities and tortuosities (f). Note that the brightest regions in (a) and (b) arise from the Zn-oxide used for sample embedding, and are therefore representative of the CLs' pore network. This Zn-oxide penetrated much less in the less-porous, dry milled sample, in which unembedded pores appear darker but are still accounted for in the 3D reconstructions, pore size distributions and porosity and tortuosity determinations in this figure.

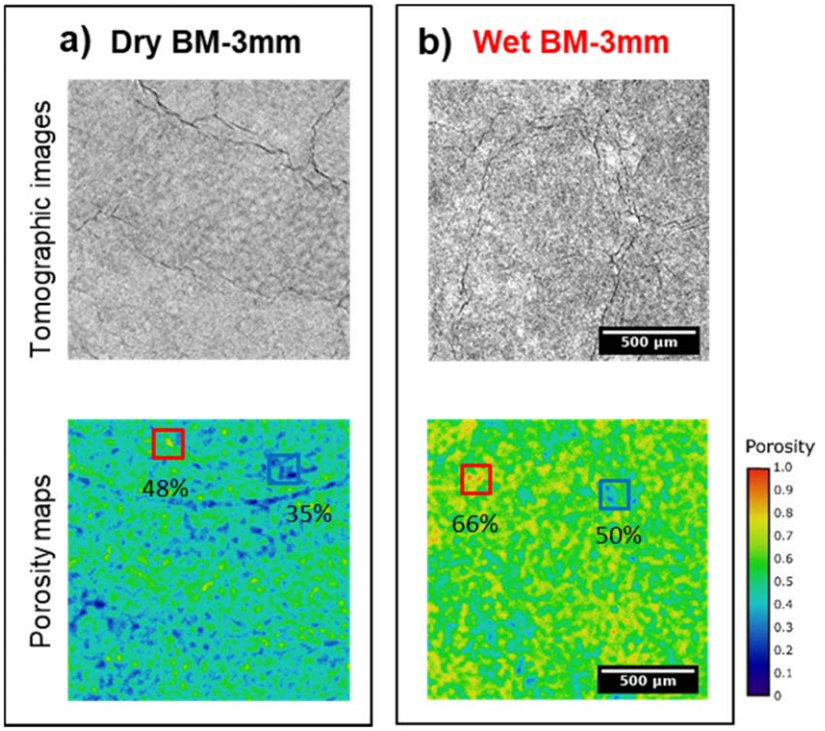

Figure 5. Tomographic images and total porosity maps of the CLs prepared from the wet BM-3mm and (a) dry BM-3mm (b) samples within a characterization area of 2.25 mm^2 (1.50 mm $\times$ 1.50 mm). Regions with significantly different porosities (150 μm $\times$ 150 μm in size) are marked in each porosity map, and the corresponding figures stand for the porosity values at those locations. Note that thickness of each tomographic slice is 3.6 μm.

Following this important verification, the properties of the CLs prepared with these two NNMCs just after their spraying (and without being submitted to compressive forces possibly induced by PEMFC-assembly) were evaluated in more detail by FIB-SEM tomography. This revealed that the CLs prepared with the "dry BM-3 mm" and "wet BM-3 mm" samples (featured in Fig. 4a vs 4b, respectively) possess significantly different morphologies; more precisely, numerous large aggregates with diameters >1 μm can be spotted in the reconstructed image of "dry BM-3 mm" (Fig. 4c), but are completely nonexistent in the CL prepared with "wet BM-3 mm" (Fig. 4d). This absence of large particles in the "wet BM-3 mm" sample results in a shift of its pore size distribution towards pores >200 nm in width (as compared to "dry BM-3 mm" sample—Fig. 4e) that are crucial for enhanced molecular diffusion of O_2 along the CLs in PEMFCs.[56] Although for thinner Pt/C CLs (whose typical pore size is up to ≈180 nm[57,58]) the main limiting factor to achieve effective mass transport is local diffusion through the ionomer/catalyst interface,[56,59] in the case of thick NNMC layers bulk molecular diffusion through meso- and macro-pores (together with Knudsen diffusion, mainly related to the transport resistance inside micropores) is much more impactful for optimum mass transport.[13] Moreover, based on the analysis of ≈10^3 μm^3 volumes, the overall porosities of the CLs were ≈57 vs ≈80% for the "dry BM-3 mm" vs "wet BM-3 mm" samples, respectively (Fig. 4f), signifying the importance of the absence of large particles for obtaining a highly porous CL. In the literature, a wide range of porosity values (from ≈30% to ≈70%) obtained by different methods have been reported for various NNMC layers.[12,55,60] In addition, the tortuosity of the CL prepared with the "wet BM-3 mm" NNMC was estimated to account to ≈1.5, which is much lower than the value of ≈2 estimated for the "dry BM-3 mm" CL as well as the ones reported for other NNMC layers (≈2–5).[12,55]

Complementarily to the FIB-SEM measurements, the geometric features of both CLs were also assessed by X-ray tomography (XTM—again, in the absence of external compression), which has recently been used to analyze the porosity and morphologhy of the micro-porous layers (MPLs) in various commercial GDLs.[61,62] The advantage of this method over FIB-SEM is that it allows the analysis of much larger volumes (herein, ≈10^6 μm^3, and thus ≈3 orders of magnitude larger than the ≈10^3 μm^3 assessed by FIB-SEM) while also providing information on the lateral homogeneity of the probed samples. Figure 5 then displays in-plane tomographic images of both samples within an area of 1.50 mm $\times$ 1.50 mm, along with their porosity maps from which we inferred average CL-porosities of ≈40 vs ≈60% for the "dry BM-3 mm" vs "wet BM-3 mm" samples, respectively. These values are ≈20% lower than those derived on the basis of the FIB-SEM measurements discussed above (cf Fig. 4f), possibly due to the large differences between the volumes probed with each technique (*vide supra*). In this regards, the XTM images in Fig. 5 unveil the presence of localized, 150 μm $\times$ 150 μm areas within both materials' CLs, with porosities remarkably higher or lower than the average values over the complete CL-areas discussed above. Although these images indicate some extent of heterenogeneity in the porosity of both catalysts' CLs, the color map of the "wet BM-3 mm" layer (cf Fig. 5b) is qualitatively similar to the one of MPLs (e. g., Freudenberg H23C10) that were categorized as homogenous in Ref. 61. Moreover, it is visually clear that the color map of the "wet BM-3 mm" layer generally features porosities >60% (and locally up to ≈80%) in most regions, whereas the one prepared with the "dry BM-3 mm" NNMC displays numeorus blue areas corresponding to porosities ⩽20% (cf Fig. 5a).

Finally, cross-sections of both catalyst layers (with loadings of ≈1 $mg_{NNMC}\,cm^{-2}$, corresponding the CL-thicknesses of ≈20–-30 μm) were also analyzed by STEM-HAADF imaging and EDS measurements, from which we inferred the ionomer distributions. The acquired Images, fluorine (F) maps and corresponding F-content profiles across the layers are displayed in Fig. 6, and close-up images including F and Fe maps are given in Fig. S10. Interestingly, these images unveil that the large catalyst particles in the "dry BM-3 mm" sample (as seen in Figs. 6a and S9b) possess a heterogeneously-distributed amount of broadly sized Fe-nanoparticle and are devoid of an F-signal within their internal pores (Fig. 6c), thus indicating that the ionomer cannot percolate through these large but highly microporous particles. Moreover, numerous >100 nm large clumps and strands of material bridging catalyst aggregates were found in the "dry BM-3 mm" CL images (see the red arrow in Fig. S10b for an example), which could be correlated with a strong F-signal and is therefore likely indicative of the presence of large ionomer strands and agglomerates between catalyst aggregates. The combination of these accumulations and of the internally ionomer-free catalyst

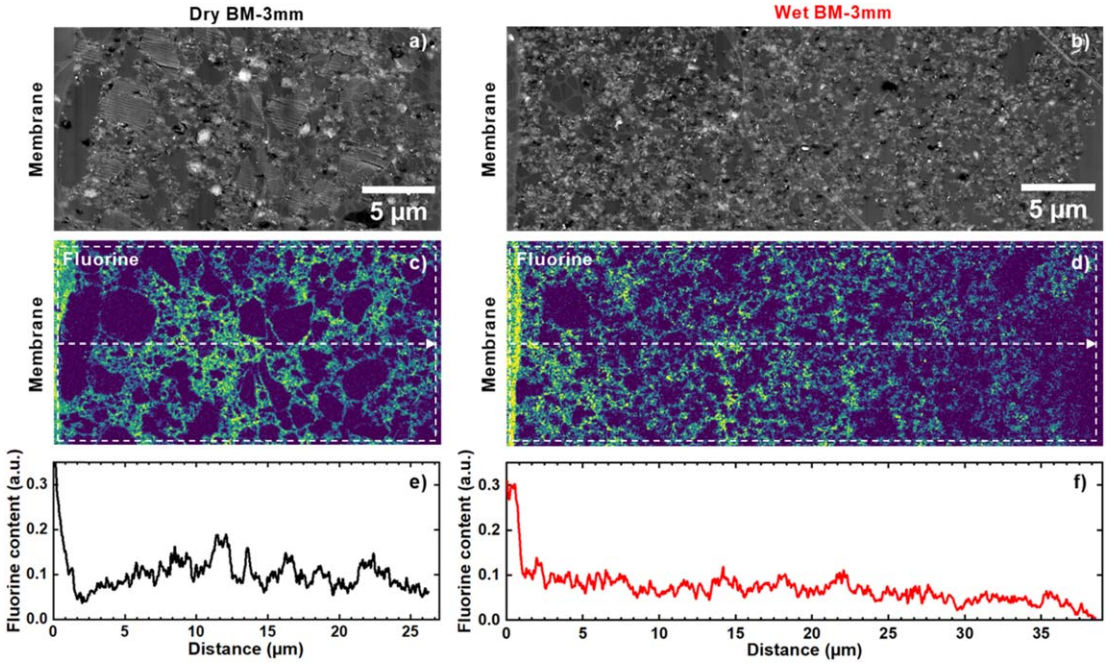

Figure 6. Cross section HAADF-STEM image of catalyst layers prepared with the dry BM-3mm (a) and wet BM-3mm (b) NNMCs, along with the corresponding fluorine EDS elemental maps and F-contents along the thickness direction of the CLs for the dry BM-3mm (c, e) and wet BM-3mm (d,f) NNMCs, respectively. Note that all images are oriented with the membrane on their left.

particles explains the large variability of the F-content seen in the line profile along this CL's cross-section, displayed in Fig. 6e. By comparison, the cross-section images acquired on the "wet BM-3 mm" CL feature a smaller variation of the ionomer-related F-content along the sample's thickness. Only few ionomer strands were observed, which were much smaller than in the "dry BM-3 mm" (see Fig. S10c), indicating that the ionomer would be mostly featured covering the catalyst's aggregates.

Effect of the NNMC aggregate size on the H_2/Air PEMFC performance.—Following the characterization of the low-loaded CLs (≈1 $mg_{NNMC}\,cm^{-2}$) prepared with the two catalysts, we prepared additional CCMs with a higher loading of ≈4 $mg_{NNMC}\,cm^{-2}$ in order to investigate the effect of the NNMC loading on the PEMFC performance. The polarization curves measured with O_2 or air as the cathode feeds and the corresponding Tafel plots are provided in Fig. S11. Notably, once the mass activity recorded in H_2/Air was translated to an O_2 partial pressure of 1 bar using Eq. 1,[29] both catalysts displayed similar mass and O_2 partial pressure normalized ORR-activities (at 0.8 V) at both loadings and irrespectively of the reactant gas (i.e., O_2 vs air − see Table SII). Despite this similarity and the minimum performance differences among catalysts observed with pure O_2 as the cathode reactant (see also Fig. 3c), the "wet BM-3 mm" sample displayed a considerably better high current density performance than the "dry BM-3 mm" one at both loadings when air (instead of O_2) was fed to the cathode (see Figs. 7a and S11a,c). Moreover, while for the "wet BM-3 mm" sample, the 4-fold loading increase resulted in a significant improvement in the high current H_2/Air performance, this higher loading resulted in the opposite effect in the case of the dry BM sample (see Figs. 7a and S11). Finally, comparing the best-performing loadings and corresponding polarization curves for each catalyst, the decrease in aggregate size brought along by wet ball milling led to ≈2-fold improvement in peak power density (see the comparison among wet- and dry-milled CLs with 4 vs 1 $mg_{NNMC}\,cm^{-2}$ loadings, respectively, in Fig. S11e).

To unveil the reasons for these differences in H_2/Air PEMFC performance among both NNMCs and as a function of their loading (see Fig. 8a, we aimed to decouple the contributions of different overpotential (η) terms to the overall cell potential (E_{cell}) conveyed by Eq. 2:[63]

$$E_{cell} = E_{rev} - i \cdot R_{HFR} - i \cdot R^{eff}_{H^+,cathode} - \eta_{ORR} - \eta_{tx} \qquad [2]$$

where E_{rev} is the thermodynamic equilibrium potential (in turn a function of the gases' partial pressures and PEMFC temperature),[64] R_{HFR} corresponds to the sum of membrane H^+-conduction resistance and contact and bulk electronic resistance that can be determined by the high frequency resistance (HFR) in impedance measurements, i is the applied current density, $R^{eff}_{H^+,cathode}$ is the effective H^+-conduction resistance of the cathode catalyst layer which allows to determine the voltage loss due to the H^+-conduction resistance across the cathode, η_{ORR} is the cathodic kinetic ORR-overpotential, and η_{tx} is the mass transport over-potential caused by O_2 concentration gradients in the electrode due to gas transport resistances. Note that Eq. 2 relies on the assumption that kinetic and transport overpotentials for the hydrogen oxidation reaction at Pt/C anode are negligible.[65]

To this end, we first aimed to estimate the H^+-conduction resistance across the thickness of NNMC layers by performing impedance measurements at the same conditions that are applied for recording the above H_2/Air polarization curves but with N_2 as the cathode gas feed.[66,67] As further discussed below, this H^+-conduction resistance can be generally quantified from the 45° degree line of the resulting Nyquist plots by applying the so-called transmission line model (TLM), whereby the difference between the low- and high-frequency resistance account for one third of the H^+-conduction resistance in the cathode electrode[30] (plus a ζ correction factor depending on the Tafel slope—*vide infra*).[63] When applying the same methodology to our NNMC layers, the Nyquist plots recorded in H_2/N_2 at 0.2 V on the high- and low-loading "wet BM-3 mm" CLs feature the expected 45° line and can be reasonably well fitted (see Fig. S12). In the case of the "dry BM-3 mm" CL, however, the same high-frequency areas of the Nyquist plots significantly deviate from the ideal 45° line, featuring instead a ≈30° slope that has been attributed to an agglomerated CL structure and a non-uniform distribution of the ionomer along its thickness.[68,69] Malko et al.[70] reported that NNMC-layers with too

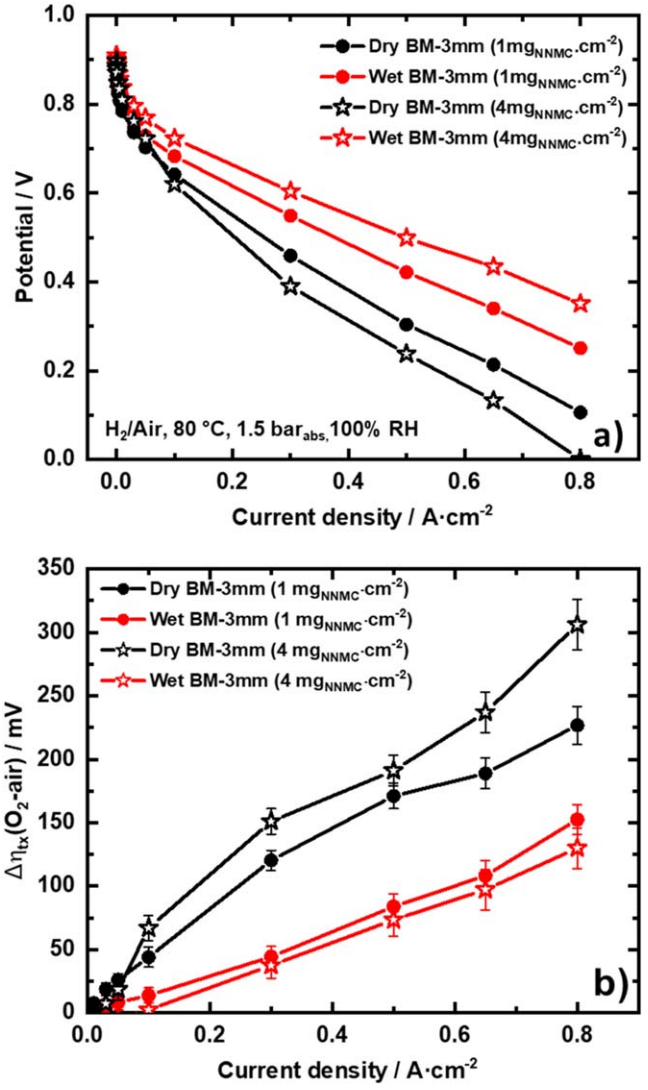

Figure 7. H_2/Air polarization curves measured in a PEMFC at 1.5 bar_{abs}, 80 °C and 100% relative humidity for MEAs fabricated with the "dry BM-3mm" or "wet BM-3mm" NNMCs using loadings of 1 or 4 $mg_{NNMC}\,cm^{-2}$ (a). Mass transport losses calculated from the difference between the polarization curves recorded with air vs O_2 as the cathode reactant gas, and corrected for the concomitant shift in the reversible potential and the kinetic overpotential due to the change in the partial pressure of O_2 when switching from O_2 to air (i.e., $\Delta\eta_{tx}$(O_2-air)—see Eqs. 4–6) (b).

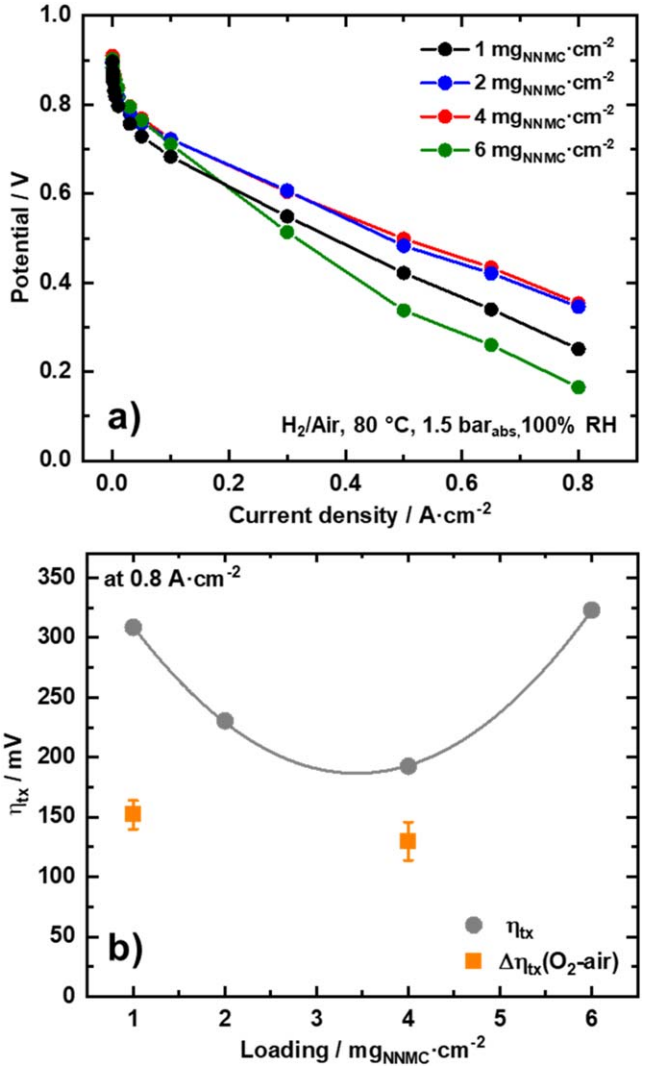

Figure 8. H_2/Air polarization curves measured in a PEMFC for the CLs fabricated with the wet BM-3mm NNMC at different loadings (a). Mass transport overpotentials obtained at 0.8 A cm^{-2} by two different approaches (b). η_{tx} is obtained by overpotential deconvolution of the polarization curves in Fig. 7a (i.e., based on the difference between the Tafel line (with an assumed slope of 70 mV dec^{-1}) and the actual polarization curves corrected for all ohmic losses (iR_{HFR} and $\Delta V_{H+,cathode}$). $\Delta\eta_{tx}$ *(O_2- air)* is estimated from the difference between polarization curves recorded with air vs O_2 as the cathode reactant gas, and corrected for the concomitant shift in the reversible potential and η_{ORR}using Eqs. 3–6.

much ionomer also tend to feature Nyquist plots with ≈30° slopes at high frequencies, likely due to an accumulation of this ionomer among the space in-between the catalyst particles similar to the one observed in our HAADF-STEM measurements (see the discussion above and Fig. 6). Alternatively, this may also be caused by limitations in the accessibility of protons to the inner parts of the large agglomerates in this "dry BM-3 mm" sample, which is not considered by the TLM.

On top of this, the TL-model also relies on the assumption that the electrical resistance of the cathode CL ($R_{e,cathode}$) is negligible when compared to its H^+-conduction resistance ($R_{H+,cathode}$), as it is generally the case for Pt/C CLs.[69,71] However, Damjanović et al. have recently discussed that this high electric conductivity condition may not be systematically applicable to NNMC layers,[51] and thus we determined the electrical resistivity (ρ_e) of our CLs by four-point probe measurements using the methodology applied in the same work[51] (whereby the properties of the samples used to measure ρ_e for both CLs are summarized in Table SIII). Based on the ρ_e values measured for the "dry BM-3 mm" and "wet BM-3 mm" (4.9 ± 0.3 vs 3.7 ± 0.1 Ω cm, respectively) CLs, the corresponding $R_{e,cathode}$ of the respective CLs with loadings of 1 vs 4 $mg_{NNMC}\,cm^{-2}$ should account to ≈10 vs ≈35 mΩ cm^2 (see Table SIV), which is in line with what Damjanović et al. reported for their CLs based on a commercial NNMC (featuring ≈6 to ≈33 mΩ cm^2 for catalyst loadings of 1 to 4 $mg_{NNMC}\,cm^{-2}$).[51] Therefore, the non-ideal impedance response of the "dry-BM-3 mm" CL cannot be attributed to its high electrical resistance. Most importantly, this also implies that the H^+-conduction resistance of this sample's CLs cannot be estimated based on a simple TLM analysis of the impedance spectra, which in terms invalidates the possibility to determine their mass transport overpotentials by isolating this term in Eq. 2.

Therefore, to be able to compare the mass transport properties of the "wet BM-3 mm" and "dry BM-3 mm" CLs at high and low loadings, we assessed their mass transport overpotentials by subtracting the polarization curves recorded in O_2 vs air (in Figs. S11a, 11c) while accounting for the shift in reversible potential and kinetic overpotential caused by the concomitant change in the O_2 partial

pressures entailed by this change of the reactant gas.[72] More precisely, switching the cathode feed from O_2 to air while keeping all other operating conditions constant (i.e. cell temperature, absolute pressure, relative humidity, reactants flow), the difference in H_2/O_2 vs H_2/Air cell potentials at a given current can be described as follows:

$$E_{cell,O2} - E_{cell,air} = E_{rev,O2} - E_{rev,air} - i \cdot R_{HFR,O2} + i \cdot R_{HFR,air} - i \cdot R^{\text{eff}}_{\text{H}^+cathode,O2} + i \cdot R^{\text{eff}}_{\text{H}^+cathode,air} - \eta_{ORR,O2} + \eta_{ORR,air} - \eta_{tx,O2} + \eta_{tx,air} \quad [3]$$

Assuming that the effective H^+-conduction resistances of the NNMC layers in O_2 vs air are similar (i.e. $R^{\text{eff}}_{\text{H}^+cathode,O2} = R^{\text{eff}}_{\text{H}^+cathode,air}$), the difference between mass transport overpotentials in H_2/O_2 and H_2/Air ($\Delta\eta_{tx}(O_2\text{-}air)$) at a given loading can be estimated from the difference in cell potentials in O_2 and air (in this study, using freshly prepared MEAs for each measurements) and the calculated shifts in E_{rev} and η_{ORR} (ΔE_{rev} vs $\Delta\eta_{ORR}$, respectively) using the following equations:

$$\Delta\eta_{tx}\ (O_2\ -\ air) = \eta_{tx,O2} - \eta_{tx,air} = \Delta E_{cell,} - \Delta(i \cdot R_{HFR}) - \ \cdot E_{rev} - \ \cdot \eta_{ORR} \quad [4]$$

$$\Delta E_{rev} = \frac{RT}{zF} \ln \frac{p_{O2}}{p_{air}} \quad [5]$$

$$\Delta\eta_{ORR} = \gamma \frac{RT}{\alpha F} \ln \frac{p_{O2}}{p_{air}} \quad [6]$$

where R = 8.314 J K^{-1} mol^{-1}, T = 353.15 K, z = 4, F = 96485 C mol^{-1}, p_{O2}/p_{air} = 4.76, α is the ORR transfer coefficient (assumed to be equal to 1, as to match the Tafel slope of 70 mV.dec^{-1} at 80 °C observed in our measurements—see cf Figs. 3d, S5b and S11), and γ is the kinetic reaction order with respect to the O_2-partial pressure at constant overpotential, with an assumed value of 0.5 in Ref. 29.

The corresponding plots of $\Delta\eta_{tx}(O_2\text{-}air)$ as a function of potential for the CLs prepared with the "wet BM-3 mm" and "dry BM-3 mm" NNMCs and at the two different loading used herein are displayed in Fig. 8b. These confirm that increasing the loading of the "dry BM-3 mm" CL from 1 to 4 mg_{NNMC} cm^{-2} resulted in a larger mass transport overpotential, possibly because the low CL-porosity and high tortuosity inferred from the above XTM and FIB-SEM measurements at 1 mg_{NNMC} cm^{-2} further aggravate the mass transport limitations featured by this NNMC when its loading (and corresponding CL thickness) is increased to 4 mg_{NNMC} cm^{-2}. By comparison, the difference between the mass transport overpotentials in O_2 and air remained roughly unchanged when the loading of the wet-milled CLs was increased 4-fold—a remarkably different behaviour that is studied in more detail in the next and final section.

Decoupling the mass transport overpotential of wet-milled CLs with different loadings.—To better understand the effect of the NNMC-loading on the mass transport overpotential of the CLs prepared with "wet-BM-3 mm," we performed additional PEFC-measurements with loadings of 2 and 6 mg_{NNMC} cm^{-2}. Interestingly, a significant improvement in the PEMFC performance was obtained by doubling the catalyst amount from 1 to 2 mg_{NNMC} cm^{-2}, but further increasing the loading to 4 mg_{NNMC} cm^{-2} barely improved the performance, which drastically decreased for the CL with 6 mg_{NNMC} cm^{-2} (see Fig. 8a). Notably, the improvement observed by increasing the loading from 1 to 2 mg_{NNMC} cm^{-2} is qualitatively consistent with previous observations for other NNMC layers,[51] and this agreement with the literature is also applicable to the subsequent performance loss observed at higher loadings. As an example of this, Shen et al.[52] reported that the PEMFC performance of their NNMC layers deteriorated at loadings >3.9 mg_{NNMC} cm^{-2}, while Banham et al.[7] obtained worse performances for their NNMC with loadings >2.5 mg_{NNMC} cm^{-2}. Additionally, this also implies that the optimum loading for each NNMC layer depends on the NNMC aggregate size and its CL morphology, which determines the magnitude of the H^+-conduction resistance and mass transport overpotential that regulate the cell output at high currents.[13,73]

In order to quantitatively differentiate the contributions of these two effects (i.e., H^+-conduction vs mass-transport resistances) to the CLs' overall performance, the $R_{H+,cathode}$ contributions of the "wet BM-3 mm" layers were determined from the fits of the impedance spectra recorded in H_2/N_2 by applying the TLM. As briefly described above, even if the Nyquist plots of the "wet BM-3 mm" layers with different loadings displayed reasonable fits to the TLM (Fig. S13), the precise $R_{H+,cathode}$ values can only be obtained when the ratio between electrical and H^+-conduction resistances ($R_{e,cathode}/R_{H+,cathode}$) is $\leqslant 10^{-2}$.[71] Thus, we calculated these $R_{e,cathode}/R_{H+,cathode}$ ratios (listed in Table SV), and found that they are systematically $\leqslant$0.05 for all loadings, implying that the difference between the true and the apparent $R_{H+,cathode}$ value inferred by the TLM-fits is at most 10%.[71] Notably, increasing the loading >2 mg_{NNMC} cm^{-2} led to a ≈4-fold increase in $R_{H+,cathode}$ (from ≈300 to 1100 mΩ cm^2 for NNMC-loadings of 1 and 2 vs 4 and 6 mg_{NNMC} cm^{-2}, respectively), in good agreement with the H^+-conduction resistances reported for NNMC layers with similar loadings.[52] Moreover, we also observed an increase of the HFR for the CLs with higher loadings of 4 and 6 mg_{NNMC} cm^{-2}; this is known to be caused by a contribution of the $R_{H+,cathode}$-term to the R_{HFR} of thick CLs (Table SV), and is again in line with previous reports for NNMC layers.[51]

Following this quantification of $R_{H+,cathode}$ for the CLs with different NNMC-loadings based on the wet BM-3 mm procedure, their polarization curves can be corrected for the voltage losses associated with the H^+-conduction resistance (ΔV_{H^+})by using the approach described by Neyerlin et al.:[63]

$$\Delta V_{\text{H}^+,cathode} = i \cdot R^{\text{eff}}_{\text{H}^+,cathode} \quad [7]$$

$$R^{\text{eff}}_{\text{H}^+,cathode} = \frac{R_{\text{H}^+,cathode}}{3 + \zeta} \quad [8]$$

where ζ is a dimensionless correction factor that depends on the product of current density and the H^+-conduction resistance divided by the intrinsic Tafel slope of the ORR (b), (i.e., on $(i \cdot R_{\text{H}^+,cathode})/b$), and that can be found in Fig. 2 of Ref. 63. We note in passing that this analysis assumes that the ORR on these NNMCs can be described through simple Tafel kinetics, and was originally formulated for ≈10 μm thick Pt/C CLs for which O_2 mass transport losses along the larger pores in the CL can be considered negligible with regards to those in the ≈20-fold thicker diffusion media. Regarding the former aspect, and in the context of the ORR on NNMCs, two different Tafel slopes of 70 or 140 mV dec^{-1} (at 80 °C) were considered in this analysis, as to account for the effect of the potential on the availability of ORR-active sites.[74] Thus, we estimated $R^{\text{eff}}_{\text{H}^+,\text{cathode}}$ by calculating ζ for both Tafel slopes, and plotted the corresponding $\Delta V_{\text{H}^+,cathode}$ values as a function of current density in Fig. S14. At low currents ($\leqslant$100 mA cm^{-2}), ΔV_{H^+} is essentially the same when assuming Tafel slopes of either 70 or 140 mV dec^{-1}; however, the difference between the $\Delta V_{\text{H}^+,cathode}$ values estimated for each Tafel slope increases at higher current densities, especially for NNMC-loadings >2 mg_{NNMC} cm^{-2} (i.e. $\Delta V_{H^+,cathode}$ ≈10 mV for loadings of 1 or 2 mg_{NNMC} cm^{-2} vs ≈40 mV for 4 or 6 mg_{NNMC} cm^{-2} at 0.8 A cm^{-2}). In order to correct the polarization curves shown in Fig. 7a for this $\Delta V_{H^+,cathode}$-term over the entire current density range, a specific Tafel slope has to be selected. Since the difference in $\Delta V_{\text{H}^+,cathode}$ calculated for the 70 and 140 mV dec^{-1} are quite significant, especially at high currents associated with larger mass transport losses, the polarization curves in Fig. 7 were corrected for the

$\Delta V_{H^+,cathode}$values obtained assuming Tafel slopes of either 70 or 140 mV dec^{-1}, and the resulting Tafel plots appear plotted in Figs. S15a and S15b, respectively. To make this interpretation more quantitative, the values of η_{tx} for each loading were estimated from the potential difference between the extrapolated Tafel lines corrected for all ohmnic losses (i.e., iR_{HFR}- and $\Delta V_{H^+,cathode}$-corrected − cf Figs. S15a and S15b that are plotted considering Tafel slopes of 70 or 140 mV dec^{-1} in the quantification of $\Delta V_{H^+,cathode}$). The corresponding η_{tx} values calculated for each Tafel slope and for the differently loaded CLs are showcased in Figs. S16a and S16b.

Following this approach, Fig. 7b features the mass transport overpotential (η_{tx}) at a current of 0.8 A cm^{-2} for the wet-milled NNMC layers with different loadings derived from this approximate overpotential deconvolution and assuming a Tafel slope of 70 mV dec^{-1}, as well the transport related overpotential deduced above from the difference between H_2/O_2 and H_2/Air performance curves (i.e., the $\Delta\eta_{tx}$ *(O_2-air)* term in Fig. 7b). The results unveil that η_{tx} decreased monotonically (from ≈320 to ≈200 mV) as the loading increased from 1 to 4 mg$_{NNMC}$ cm^{-2} despite the ≈4-fold boost of the CL-thicknesses entailed by this approach. This decrease of the mass transport losses with higher loadings can be explained by invoking an improvement of the CLs' mass transport properties with increasing roughness factors (i.e., with the number of ORR-active sites, directly proportional to the catalyst loading), as it has been observed for Pt–based CLs.[75,76] However, this beneficial effect is eventually counteracted by a deterioration of molecular and Knudsen diffusion within thick CLs,[13] which in the case of our NNMCs appears to prevail for NNMC loadings >4 mg$_{NNMC}$ cm^{-2} (corresponding to CL-thicknesses >100 μm).

Besides for this effect, it is also worth noting that the magnitude of $\Delta\eta_{tx}$ *(O_2- air)* is systematically lower than that of η_{tx} for any given loading (cf Fig. 7). In this regard, the η_{tx} term obtained via overpotential deconvolution can only be equal to $\Delta\eta_{tx}$ *(O_2- air)* (i.e., the difference between η_{tx} obtain in H_2/Air and H_2/O_2) only if η_{tx}^{O2} (i.e. the mass transport overpotential in H_2/O_2) is negligible. This seemed to be the case for the very thin $PtNi_3$ aerogel CLs[72] characterized by Henning et al., whereas the contribution of η_{tx}^{O2} to the cell potential might not be negligible for NNMC layers. This was confirmed by estimating the value of η_{tx}^{O2} from the H_2/O_2 polarization curves in Fig. S11 via a similar overpotential deconvolution approach (see the results in Fig. S17a), since the difference between η_{tx} and $\Delta\eta_{tx}$ *(O_2- air)* matched well with the η_{tx}^{O2} values obtained for the CLs with 1 or 4 mg$_{NNMC}$ cm^{-2} (i.e., 160 vs 60 mV, respectively).

Finally, we also verified that the relation between NNMC-loading and mass transport overpotential values inferred from this deconvolutive approach are qualitatively similar when these terms are assessed assuming a higher Tafel slope of 140 mV dec^{-1}.[53,74] In this regard, Fig. S18 shows the loading-dependent values of η_{tx} and $\Delta\eta_{tx}$ *(O_2- air)* calculated by assuming a Tafel slope as 140 mV dec^{-1}, and compares them with the ones for a Tafel slope of 70 mV dec^{-1} (in cf Fig. 7b). In addition, we also calculated η_{tx}^{O2} for a Tafel slope of 140 mV dec^{-1} (Fig. S19a), but in this occasion we did not observe a good match between η_{tx}^{O2} and $\Delta\eta_{tx}$ (Fig. S19b), unlike in the case of a 70 mV dec^{-1} slope (cf Fig. S17b).

Conclusions

In summary, by substituting the dry ball milling (BM) used in our previous NNMC synthesis with wet BM, we efficiently reduced the catalyst's aggregate size from >5 μm to ≈100 nm as to yield a material with a significantly improved PEMFC performance. The properties of CLs fabricated with two NNMCs having different aggregate size ("dry BM-3 mm" and "wet BM-3 mm") were extensively studied by FIB-SEM, XTM and STEM-EDS, which revealed that the absence of big aggregates is of paramount importance to achieve a CL with enhanced mass transport properties, possibly due to the commensurate decrease of the intra-pore diffusion lengths brought along by this diminished aggregate size. Our PEMFC results were also supportive of these observations, and thus while the small-sized "wet BM-3 mm" CLs displayed an improved PEMFC-performance upon increasing the loading from 1 to 4 mg$_{NNMC}$ cm^{-2}, the "dry BM-3mm" catalyst with big aggregates featured a poorer cell behaviour at higher NNMC-loadings. These differences were ascribed to the enhanced mass transport properties of the CLs fabricated with "wet BM-3mm" sample, which were initially assessed on the basis of the mass transport overpotential differences observed when switching the cathode feed from O_2 to air. In a subsequent step, we conducted a more rigorous overpotential deconvolution (i.e., including an impedance-based quantification of the H^+-conduction losses through the CLs) of the polarization curves recorded on CLs prepared with the "wet BM-3 mm" catalyst at NNMC-loadings of 1, 2, 4 or 6 mg$_{NNMC}$ cm^{-2}. The results indicated that increasing the loading up to 4 mg$_{NNMC}$ cm^{-2} resulted in a significant improvement of the mass transport overpotential that we ascribe to a concomitant effect on this variable on the electrodes' roughness (i.e., the number of ORR-active sites). However, this beneficial effect was outweighed by further increasing the loading to 6 mg$_{NNMC}$ cm^{-2}, which led to a higher mass transport overpotential caused by limitations in the mass transport of the gases through such a thick CL.

Acknowledgments

We would like to thank SuperXAS beamline at the Swiss Light Source for allowing us to use their facilities and Adam H. Clark for helping with the XAS measurements. We also acknowledge Felix N. Büchi for insightful discussions.

ORCID

Anne Berger https://orcid.org/0000-0003-3230-4730
Hubert A. Gasteiger https://orcid.org/0000-0001-8199-8703
Vasiliki Tileli https://orcid.org/0000-0002-0520-6900
Juan Herranz https://orcid.org/0000-0002-5805-6192

References

1. M. J. O'Malley et al., *Proceedings of the IEEE*, **108**, 1437 (2020).
2. F. T. Wagner, B. Lakshmanan, and M. F. Mathias, *The Journal of Physical Chemistry Letters*, **1**, 2204 (2010).
3. D. A. Cullen, K. C. Neyerlin, R. K. Ahluwalia, R. Mukundan, K. L. More, R. L. Borup, A. Z. Weber, D. J. Myers, and A. Kusoglu, *Nat. Energy*, **6**, 462 (2021).
4. O. Gröger, H. A. Gasteiger, and J.-P. Suchsland, *J. Electrochem. Soc.*, **162**, A2605 (2015).
5. S. T. Thompson and D. Papageorgopoulos, *Nat. Catal.*, **2**, 558 (2019).
6. L. Osmieri, J. Park, D. A. Cullen, P. Zelenay, D. J. Myers, and K. C. Neyerlin, *Current Opinion in Electrochemistry*, **25**, 100627 (2021).
7. D. Banham, T. Kishimoto, Z. Yingjie, T. Sato, K. Bai, Y. Imashiro, and S. Ye, *Sci. Adv.*, **4**, eaar7180 (2018).
8. D. A. C. Hoon, T. Chung, D. Higgins, B. T. Sneed, F. H. Edward, L. M. Karren, and P. Zelenay, *Science*, **357**, 479 (2017).
9. J. Shui, C. Chen, L. Grabstanowicz, D. Zhao, and D. J. Liu, *Proc Natl Acad Sci U S A*, **112**, 10629 (2015).
10. E. Proietti, F. Jaouen, M. Lefevre, N. Larouche, J. Tian, J. Herranz, and J. P. Dodelet, *Nat. Commun.*, **2**, 416 (2011).
11. S. Stariha, K. Artyushkova, M. J. Workman, A. Serov, S. McKinney, B. Halevi, and P. Atanassov, *J. Power Sources*, **326**, 43 (2016).
12. S. Komini Babu, H. T. Chung, P. Zelenay, and S. Litster, *ACS Appl. Mater. Interfaces*, **8**, 32764 (2016).
13. G. Wang, L. Osmieri, A. G. Star, J. Pfeilsticker, and K. C. Neyerlin, *J. Electrochem. Soc.*, **167**, 044519 (2020).
14. H. Zhang et al., *J. Am. Chem. Soc.*, **139**, 14143 (2017).
15. V. Armel, J. Hannauer, and F. Jaouen, *Catalysts*, **5**, 1333 (2015).
16. S. Ratso et al., *ACS Appl. Energy Mater.*, **2**, 7952 (2019).
17. A. Uddin, L. Dunsmore, H. Zhang, L. Hu, G. Wu, and S. Litster, *ACS Appl. Mater. Interfaces*, **12**, 2216 (2020).
18. A. Serov, K. Artyushkova, E. Niangar, C. Wang, N. Dale, F. Jaouen, M.-T. Sougrati, Q. Jia, S. Mukerjee, and P. Atanassov, *Nano Energy*, **16**, 293 (2015).
19. K. Ebner, J. Herranz, V. A. Saveleva, B.-J. Kim, S. Henning, M. Demicheli, F. Krumeich, M. Nachtegaal, and T. J. Schmidt, *ACS Appl. Energy Mater.*, **2**, 1469 (2019).
20. F. Jaouen et al., *ACS Appl. Mater. Interfaces*, **1**, 1623 (2009).
21. F. Jaouen, M. Lefèvre, J. P. Dodelet, and M. Cai, *J. Phys. Chem. B*, **110**, 5553 (2006).

22. M. Lefèvre, E. Proietti, F. Jaouen, and J. P. Dodelet, *Science*, **324**, 71 (2009).
23. U. I. Kramm et al., *Phys. Chem. Chem. Phys.*, **14**, 11673 (2012).
24. H. Shin, S. Lee, H. S. Jung, and J.-B. Kim, *Ceram. Int.*, **39**, 8963 (2013).
25. X. Yin, L. Lin, H. T. Chung, S. Komini Babu, U. Martinez, G. M. Purdy, and P. Zelenay, *ECS Trans.*, **77**, 1273 (2017).
26. M. Povia, J. Herranz, T. Binninger, M. Nachtegaal, A. Diaz, J. Kohlbrecher, D. F. Abbott, B.-J. Kim, and T. J. Schmidt, *ACS Catal.*, **8**, 7000 (2018).
27. I. Miccoli, F. Edler, H. Pfnur, and C. Tegenkamp, *J. Phys. Condens. Matter*, **27**, 223201 (2015).
28. P. Oberholzer and P. Boillat, *J. Electrochem. Soc.*, **161**, F139 (2014).
29. K. C. Neyerlin, W. Gu, J. Jorne, and H. A. Gasteiger, *J. Electrochem. Soc.*, **153**, A1955 (2006).
30. Y. Liu, M. W. Murphy, D. R. Baker, W. Gu, C. Ji, J. Jorne, and H. A. Gasteiger, *J. Electrochem. Soc.*, **156**, B970 (2009).
31. S. Ratso et al., *Renewable Energy*, **167**, 800 (2021).
32. M. Toozandehjani et al., *Materials* , **10**, 1232 (2017).
33. S. Krishna and C. M. Patel, *Mater. Lett.*, **257**, 126738 (2019).
34. G. Liu, Z. Su, D. He, and C. Lai, *Electrochim. Acta*, **149**, 136 (2014).
35. H. T. Chung, J. H. Won, and P. Zelenay, *Nat. Commun.*, **4**, 1922 (2013).
36. K. Ebner, "Fe/N/C-type Oxygen Reduction Reaction Catalysts From Synthesis to Advanced In Situ Spectroscopic Characterization." *81, ETH Zurich* (2020).
37. A. Zitolo, V. Goellner, V. Armel, M. T. Sougrati, T. Mineva, L. Stievano, E. Fonda, and F. Jaouen, *Nat. Mater.*, **14**, 937 (2015).
38. Q. Jia, E. Liu, L. Jiao, S. Pann, and S. Mukerjee, *Adv. Mater.*, **31**, e1805157 (2019).
39. K. Ebner et al., *Adv. Energy Mater.*, **12**, 2103699 (2022).
40. K. Ebner et al., *Phys. Chem. Chem. Phys.*, **23**, 9147 (2021).
41. S. Ünsal, T. J. Schmidt, and J. Herranz, *Electrochim. Acta*, **445**, 142024 (2023).
42. K. Shinozaki, J. W. Zack, S. Pylypenko, B. S. Pivovar, and S. S. Kocha, *J. Electrochem. Soc.*, **162**, F1384 (2015).
43. K. Shinozaki, J. W. Zack, R. M. Richards, B. S. Pivovar, and S. S. Kocha, *J. Electrochem. Soc.*, **162**, F1144 (2015).
44. V. Di Noto, E. Negro, A. Nale, G. Pagot, K. Vezzù, and P. Atanassov, *Current Opinion in Electrochemistry*, **25** (2021).
45. T. J. Schmidt, H. A. Gasteiger, G. D. Stab, P. M. Urban, D. M. KoIb, and R. J. Behm, *Journal of Electrochemical Society*, **145**, 2354 (1998).
46. U. A. Paulus, T. J. Schmidt, H. A. Gasteiger, and R. J. Behm, *J. Electroanal. Chem.*, **495**, 134 (2001).
47. A. Bonakdarpour, M. Lefevre, R. Yang, F. Jaouen, T. Dahn, J.-P. Dodelet, and J. R. Dahn, *Electrochem. Solid-State Lett.*, **11**, B105 (2008).
48. F. Jaouen and J.-P. Dodelet, *J. Phys. Chem. C*, **113**, 15422 (2009).
49. M. Primbs et al., *Energy Environ. Sci.*, **13**, 2480 (2020).
50. F. Jaouen, V. Goellner, M. Lefèvre, J. Herranz, E. Proietti, and J. P. Dodelet, *Electrochim. Acta*, **87**, 619 (2013).
51. A. M. Damjanović, B. Koyutürk, Y.-S. Li, D. Menga, C. Eickes, H. A. El-Sayed, H. A. Gasteiger, T.-P. Fellinger, and M. Piana, *J. Electrochem. Soc.*, **168**, 114518 (2021).
52. S. Shen, J. Chen, X. Yan, X. Cheng, L. Zhao, Z. Ren, L. Li, and J. Zhang, *J. Power Sources*, **496**, 229817 (2021).
53. L. Osmieri, A. H. A. Monteverde Videla, P. Ocón, and S. Specchia, *J. Phys. Chem. C*, **121**, 17796 (2017).
54. J. Yang, J. Li, R. Ding, C. Liu, and X. Yin, *J. Electrochem. Soc.*, **168**, 096502 (2021).
55. A. Serov, A. D. Shum, X. Xiao, V. De Andrade, K. Artyushkova, I. V. Zenyuk, and P. Atanassov, *Appl. Catalysis B*, **237**, 1139 (2018).
56. N. Nonoyama, S. Okazaki, A. Z. Weber, Y. Ikogi, and T. Yoshida, *J. Electrochem. Soc.*, **158**, B416 (2011).
57. J. Xie, K. L. More, T. A. Zawodzinski, and W. H. Smith, *J. Electrochem. Soc.*, **151**, A1084 (2004).
58. F. C. Cetinbas, R. K. Ahluwalia, N. Kariuki, V. De Andrade, D. Fongalland, L. Smith, J. Sharman, P. Ferreira, S. Rasouli, and D. J. Myers, *J. Power Sources*, **344**, 62 (2017).
59. A. Z. Weber and A. Kusoglu, *J. Mater. Chem. A*, **2**, 17207 (2014).
60. S. K. Babu et al., *J. Power Sources*, **472**, 228442 (2020).
61. Y.-C. Chen, C. Karageorgiou, J. Eller, T. J. Schmidt, and F. N. Büchi, *J. Power Sources*, **539**, 231612 (2022).
62. Y. C. Chen, A. Berger, S. De Angelis, T. Schuler, M. Bozzetti, J. Eller, V. Tileli, T. J. Schmidt, and F. N. Buchi, *ACS Appl. Mater. Interfaces*, **13**, 16227 (2021).
63. K. C. Neyerlin, W. Gu, J. Jorne, A. Clark, and H. A. Gasteiger, *J. Electrochem. Soc.*, **154**, B279 (2007).
64. D. M. Bernardi and M. V. Verbrugge, *Journal of Electrochemical Society*, **139**, 2477 (1992).
65. K. C. Neyerlin, W. Gu, J. Jorne, and H. A. Gasteiger, *J. Electrochem. Soc.*, **154**, B631 (2007).
66. M. C. Lefebvre, R. B. Martin, and P. G. Pickup, *Electrochem. Solid-State Lett.*, **2**, 259 (1999).
67. R. Makharia, M. F. Mathias, and D. R. Baker, *J. Electrochem. Soc.*, **152**, A970 (2005).
68. D. Malevich, B. R. Jayasankar, E. Halliop, J. G. Pharoah, B. A. Peppley, and K. Karan, *J. Electrochem. Soc.*, **159**, F888 (2012).
69. R. Morasch, J. Landesfeind, B. Suthar, and H. A. Gasteiger, *J. Electrochem. Soc.*, **165**, A3459 (2018).
70. D. Malko, T. Lopes, E. A. Ticianelli, and A. Kucernak, *J. Power Sources*, **323**, 189 (2016).
71. J. Landesfeind, M. Ebner, A. Eldiven, V. Wood, and H. A. Gasteiger, *J. Electrochem. Soc.*, **165**, A469 (2018).
72. S. Henning, H. Ishikawa, L. Kuhn, J. Herranz, E. Muller, A. Eychmuller, and T. J. Schmidt, *Angew. Chem. Int. Ed. Engl.*, **56**, 10707 (2017).
73. L. Osmieri et al., *Nano Energy*, **75**, 104943 (2020).
74. L. Osmieri et al., *Appl. Catalysis B*, **257**, 117929 (2019).
75. T. A. Greszler, D. Caulk, and P. Sinha, *J. Electrochem. Soc.*, **159**, F831 (2012).
76. A. Kongkanand and M. F. Mathias, *J. Phys. Chem. Lett.*, **7**, 1127 (2016).